

# Orientation Effect on the Light Curve Shape of Periodic Methanol Maser Sources

J. Morgan,<sup>1\*</sup> D.J. van der Walt,<sup>1</sup> J.O. Chibueze<sup>1,2</sup> and Q. Zhang<sup>3</sup>

<sup>1</sup>*Centre for Space Research, North-West University, Potchefstroom 2520, South Africa*

<sup>2</sup>*Department of Physics and Astronomy, Faculty of Physical Sciences, University of Nigeria, Carver Building, 1 University Road, Nsukka, Nigeria*

<sup>3</sup>*Center for Astrophysics | Harvard & Smithsonian, 60 Garden Street, Cambridge MA 02138, USA*

Accepted XXX. Received YYY; in original form ZZZ

## ABSTRACT

We report the results of our pilot millimeter observations of periodic maser sources. Using SMA, we carried out 1.3 mm observations of G22.357+0.066 and G25.411+0.105, while ALMA 1.3 mm archival data was used in the case of G9.62+0.19E. Two continuum cores (MM1 and MM2) were detected in G22.357+0.066, while 3 cores (MM1 – MM3) detected in G25.411+0.105. Assuming dust-to-gas ratio of 100, we derived the masses of the detected cores. Using the <sup>12</sup>CO (2-1) and <sup>13</sup>CO (2-1) line emission, we observed gas kinematics tracing the presence of bipolar outflows in all three star-forming regions. In the cases of G22.357+0.066 and G9.62+0.19E, both with similar periodic maser light curve profiles, the outflowing gas is seen in the north-west south-east direction. This suggest edge-on view of the 2 sources. G25.411+0.105, with a contrasting light curve profile, show a spatially collocated blue and red outflow lobes, suggesting a face-on view. Our results suggest that orientation effects may play a role in determining the characteristics of the light curves of periodic methanol masers.

**Key words:** masers – stars: formation – ISM: clouds – radio lines: ISM – sub-millimetre: ISM – techniques: interferometric

## 1 INTRODUCTION

Limitation in the number of samples of massive stars (compared to low-mass counterparts), their generally large distances from the Sun and along with being deeply embedded in their natal clouds for most of their lifetimes, impede our understanding of various evolutionary stages of massive stars. The challenges of the observational study of high-mass star formation are gradually being tackled with improved sensitivities and angular resolutions offered by new and upgraded instruments around the globe. Some of the recently resolved issues include the problem of angular momentum transfer to enable mass accretion onto the central core (young protostar). The Atacama Large Millimetre/sub-millimetre Array (ALMA) offered ideal data for detecting a disk-driven rotating bipolar outflow in Orion Source I (Hirota et al. 2017). A keplerian disk has also been detected in the massive young stellar object G11.92–0.61 MM1 (Ilee et al. 2016).

Masers are known to serve as signposts of sites for star formation, especially the 6.7 GHz class II methanol (CH<sub>3</sub>OH) masers that are known to be exclusively associated with massive stars (Breen et al. 2013). They could serve as tracers of physical conditions around forming high-mass stars. The variability of CH<sub>3</sub>OH masers was first outlined by Goedhart et al. (2004) who discovered periodicity in the flux

density variations of class II CH<sub>3</sub>OH masers. Since then, an additional 25 periodic class II methanol masers, with periods ranging between 24 and 510 days, have been discovered. An intriguing property of the sample of known periodic methanol masers is that there is no single unique shape of the light curves of these masers. It is not possible to classify all periodic masers according to the shape of their light curves, however, Maswanganye et al. (2015) suggests that there are at least two categories of periodic masers for which the light curves are rather well defined: (i) The flare profile shows a fast increase in intensity from a low state followed by a slow decrease in intensity which can be described in terms of the recombination of a hydrogen plasma from a higher to a lower state of ionization. The sources belonging to this group are G9.62+0.19E (Goedhart et al. 2003), G22.357+0.066 (Szymczak et al. 2015), G37.55+0.20 (Araya et al. 2010), and G45.473+0.134 (Szymczak et al. 2015). (ii) The variability profile resembles that of  $|\cos(\omega t)|$  function, (referred to as a Bunny hop) and is similar to that seen in some eclipsing binary systems. Sources belonging to this group are G25.411+0.105 (Szymczak et al. 2015), G339.62–0.12 (Goedhart et al. 2014), G338.93–0.06 (Goedhart et al. 2014) and G358.460–0.391 (Maswanganye et al. 2015).

Several mechanisms have been proposed to explain the periodicity of methanol masers. van der Walt et al. (2009) and van der Walt (2011) proposed a colliding wind binary (CWB) system for the periodic methanol masers in G9.62+0.20E

\* E-mail: jeanmariemorgan@gmail.com (JM)

and other periodic methanol maser sources with similar light curves. Using a more realistic model [van den Heever et al. \(2019\)](#) also showed that the CWB scenario can explain the light curves of the periodic methanol masers in G9.62+0.20E, G22.357+0.066, G37.55+0.20, and G45.473+0.134. Other mechanisms proposed are: the pulsational instabilities of very young accreting high-mass stars ([Inayoshi et al. 2013](#)), spiral shocks associated with very young binary systems orbiting within a circumbinary disk ([Parfenov & Sobolev 2014](#)), periodic accretion in a very young binary system ([Araya et al. 2010](#)), and outflows in a binary system ([Singh & Deshpande 2012](#)). [Maswanganye et al. \(2015\)](#) evoked an eclipsing binary system involving a high-mass (primary) star and a bloated low-mass (companion) star in explaining the observed periodicity of the methanol masers in G358.460-0.391. While each of the suggested mechanisms may be sufficient for explaining periodicity in individual star-forming regions, the complexity in the nature of massive star-forming environments and the uniqueness of each region, make it difficult to evoke any one of the mechanisms for all cases. In fact, different mechanisms may be responsible for the different observed flare profiles (see [van der Walt et al. 2016](#), for a discussion). However, the fact that it is possible to identify at least two groups of periodic sources (as explained above), each for which the light curves are very similar, suggests that there are some sources for which the underlying mechanism is the same. It is therefore reasonable to argue that there might be other similarities in star-forming regions that host periodic methanol masers with same light curves. In other words, the similarity in light curves might also manifest in other properties of the star-forming regions in addition to the maser emission.

To understand the cause of periodicity in class II CH<sub>3</sub>OH masers, it is imperative to probe the bulk of the gas and dust beyond the masing region which constitutes only a small fraction of the star-forming environment. Observing dust continuum and molecular line emissions of periodic maser sources could reveal some physical properties that are key to understanding periodicity in class II CH<sub>3</sub>OH maser sources.

In this paper, we present the millimetre properties of three periodic CH<sub>3</sub>OH maser sources viz., G22.357+0.066 [kinematic distance 4.86 kpc based on [Reid et al. \(2009\)](#); see also ([Szymczak et al. 2011](#))], G25.411+0.105 [kinematic distance of 9.50 kpc ([Szymczak et al. 2007](#)), while [Sridharan et al. \(2002\)](#) reported the presence of SiO, CH<sub>3</sub>OH, and CH<sub>3</sub>CN molecular lines as well as H<sub>2</sub>O and CH<sub>3</sub>OH masers.] and G9.62+0.19E [parallax distance of 5.2 kpc ([Sanna et al. 2009](#)). [Sanna et al. \(2009\)](#) also reported the presence of a 1.3 cm continuum source detected with VLA.]. G9.62+0.19E and G22.357+0.066 have the same type of flaring light curve while G25.411+0.105's light curve is of the Bunny hop type.

## 2 OBSERVATIONS

### 2.1 Submillimeter Array (SMA) Observations

The SMA<sup>1</sup> observations of G22.357+0.066 and G25.411+0.105 were carried out on June 27, 2016, and August 6, 2017. The phase center for G22.357+0.066 and G25.411+0.105 is (R.A., decl.)<sub>J2000</sub> = (18<sup>h</sup> 31<sup>m</sup> 44<sup>s</sup>.29, -09<sup>d</sup> 22<sup>m</sup> 11<sup>s</sup>.2) and (R.A., decl.)<sub>J2000</sub> = (18<sup>h</sup> 37<sup>m</sup> 16<sup>s</sup>.90, -06<sup>d</sup> 38<sup>m</sup> 30<sup>s</sup>.5), respectively with a 2// error in the pointing.

The observations in 2016 used the ASIC and SWARM correlator with seven antennas in the compact array configuration. The 8 GHz bandwidth is divided into two side-bands, lower side-band of 4 GHz and upper side-band of 4 GHz, each consisting of 128 channels. The lower side-band covered the frequency range from 212.9 GHz to 220.6 GHz and the upper side-band the frequency range from 228.7 GHz to 236.6 GHz. The calibrators and the two target sources were observed in turn, leading to a total observation time of 80 minutes for each target source. The system temperature correction was done in MIRIAD and the data was converted to CASA measurements sets. The full calibration of the data was done in CASA, with Titan as flux calibrator and 3C279 as bandpass calibrator. The antenna gain correction was done using Quasars J1733–130 and J1743–038.

The observations on August 6, 2017 used six antennas in the compact array configuration. The SWARM correlator was configured to cover 8 GHz bandwidth in lower side-band (213.5 – 221.5 GHz) and upper side-band (229.5 – 237.5 GHz), respectively. The native spectral resolution is 140 kHz per channel across the entire spectral band. The on-source time for each target is approximately 60 min. Neptune was observed for flux calibration, quasar 3C279 for bandpass calibration and quasars J1830+063 and J1743–038 for time-dependent antenna gain calibration. The raw visibilities were calibrated using the IDL superset MIR<sup>2</sup>, and exported into CASA for imaging.

The 2016 and 2017 data sets were combined in CASA and the largest recoverable scale is  $\sim 33''$ . The CASA clean task was used to produce the molecular line emission spectra of <sup>12</sup>CO, <sup>13</sup>CO and C<sup>18</sup>O with their rest frequencies at 230.53800000 GHz, 220.39868420 GHz and 219.56035410 GHz respectively. The rest frequencies were obtained from the Splatalogue catalogue; more details on the line emission parameters is given in Table 2. The channel width for all the line emission is 1.0 km s<sup>-1</sup>. Other than the CO lines, there were no significant line features above 3 $\sigma$ . The dust continuum were produced using the line-free channels. The synthesized beam size for the continuum is 6''.08  $\times$  2''.79 and 5''.80  $\times$  2''.50 for the spectral line images. The root-mean-square (rms) noise level in the continuum, <sup>12</sup>CO line images and <sup>13</sup>CO/C<sup>18</sup>O line images are  $\sim 1$  mJy beam<sup>-1</sup>, 170 mJy beam<sup>-1</sup> and  $\sim 20$  mJy beam<sup>-1</sup> respectively.

<sup>1</sup> The Submillimeter Array is a joint project between the Smithsonian Astrophysical Observatory and the Academia Sinica Institute of Astronomy and Astrophysics, and is funded by the Smithsonian Institution and the Academia Sinica.

<sup>2</sup> <https://www.cfa.harvard.edu/~cqi/mircook.html>

## 2.2 ALMA Archival Data

We obtained ALMA band 6 archival data on G9.62+0.19 (Project ID: 2013.1.00957.S) taken on 2015 April 27 (39 antennas of the 12-m main array), May 24 (34 antennas of the 12-m main array) in its compact and extended configurations, respectively. It was also observed with the Atacama Compact Array (ACA: 7-m array) on 2015 May 04 with 10 antennas. J1733–1304, J1517–2422 were used as bandpass calibration and phase calibration, respectively, while Neptune, Titan and J1733–130 were used as flux calibrators.

The Band 6 (230 GHz) receivers were used for the observations in dual-polarization mode. To cover the molecular lines  $^{12}\text{CO}$  (2-1) and  $\text{CH}_3\text{OH } v_t = 1, (6_1-7_2 \text{ A-})$ , five spectral windows with a bandwidth of 117 MHz in each window, as well as another spectral window with a bandwidth of 234 MHz, was used. The channel width in all the spectra windows is  $0.08 \text{ km s}^{-1}$ . The ALMA data was also calibrated in CASA. They combined data from three configurations in CASA, that included single dish data, with a LAS of  $\sim 20''$  for the combined data.

The continuum image has a rms noise of  $1.0 \text{ mJy beam}^{-1}$  and a synthesized beam of  $0''.94 \times 0''.71$ . For the molecular lines the rms noise is  $\sim 20 \text{ mJy beam}^{-1}$ . The lines  $^{12}\text{CO}$  (2-1) and  $\text{CH}_3\text{OH } v_t = 1, (6_1-7_2 \text{ A-})$  has synthesized beam sizes of  $0''.94 \times 0''.73$  and  $0''.99 \times 0''.72$  respectively. The rest frequency used for  $\text{CH}_3\text{OH } v_t = 1, (6_1-7_2 \text{ A-})$  was 217.29920 GHz and was also obtained from the Splatalogue; the details on the line parameters can be found in Table 2. More details of the observations can be found in Liu et al. (2017).

## 3 RESULTS

### 3.1 G22.357+0.066

#### 3.1.1 1.3 mm Continuum Emission: G22.357+0.066

Two millimetre continuum cores (MM1 & MM2) associated with G22.357+0.066, which is located at a distance  $4.86 \pm 0.3 \text{ kpc}$  (Reid et al. 2009), were detected in the SMA observations and are presented in Figure 1. The root-mean-square (rms) noise level in the continuum image of G22.357+0.066 is  $\sim 1 \text{ mJy beam}^{-1}$ . Table 1 presents the peak positions (RA and Dec), the peak and integrated flux densities for each detected continuum object. MM1 is the only resolved core. MM2 is marginally resolved with an angular size of  $6''.8 \times 3''.1$ . MM2 is located  $\leq 16''$ , south-west of MM1. Using the methanol multi-beam (MMB) survey position of the masers, we found it to be located  $\sim 0''.2$  from the peak continuum emission of MM1 (see Figure 1).

The dust mass,  $M_d$ , can be estimated from

$$M_d = \frac{S_\nu D^2}{\kappa_\nu B_\nu(T_d)} \quad (1)$$

assuming optically thin dust emission (Hildebrand 1983).  $S_\nu$  is the continuum flux density at frequency,  $\nu$ ,  $B_\nu(T_d)$  is the Planck function at dust temperature,  $T_d$ ,  $D$  is the distance to the source and  $\kappa_\nu$  the dust opacity per unit mass,  $\kappa_\nu = 0.19 \text{ cm}^2 \text{ g}^{-1}$  at 230 GHz (Weingartner & Draine 2001). Observations indicate that star-forming regions that have no signs of an H II regions, but that are associated with masers have temperatures of  $\sim 20 \text{ K}$  (Wu et al. 2006; Urquhart et al. 2011; Lu et al. 2014). Thus we adopted a dust temperature,  $T_d$ , of

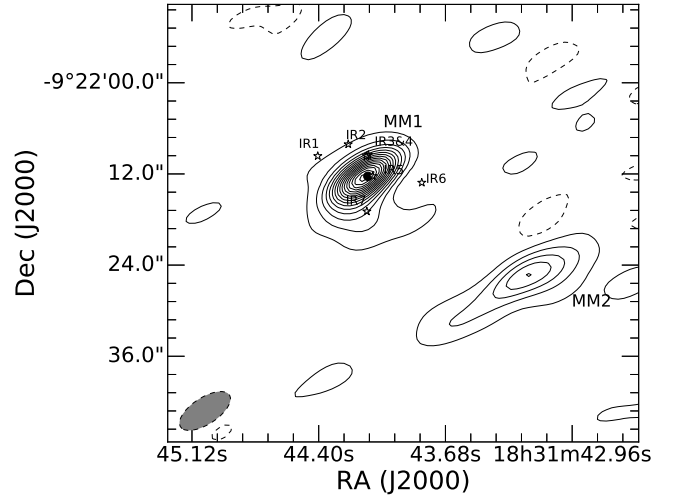


**Figure 1.** G22.357+0.066: 1.3 mm continuum emission with the near infra-red (NIR) counterparts (star symbol) obtained from UKIDSS Consortium (2012) within a radius of  $5''$  from the maser. MM1 and MM2 indicates each millimetre object detected in the SMA observation. The dust contour levels are  $[-3, 3, 9, 15, 21, 27, 33, 39, 45, 51, 57, 63, 69, 75, 81, 87, 93] \times \sigma \text{ mJy beam}^{-1}$ , where  $\sigma$  is  $1 \text{ mJy beam}^{-1}$  and the circle shows the position of the periodic methanol maser which has a positional uncertainty of  $\sim 6''$ .

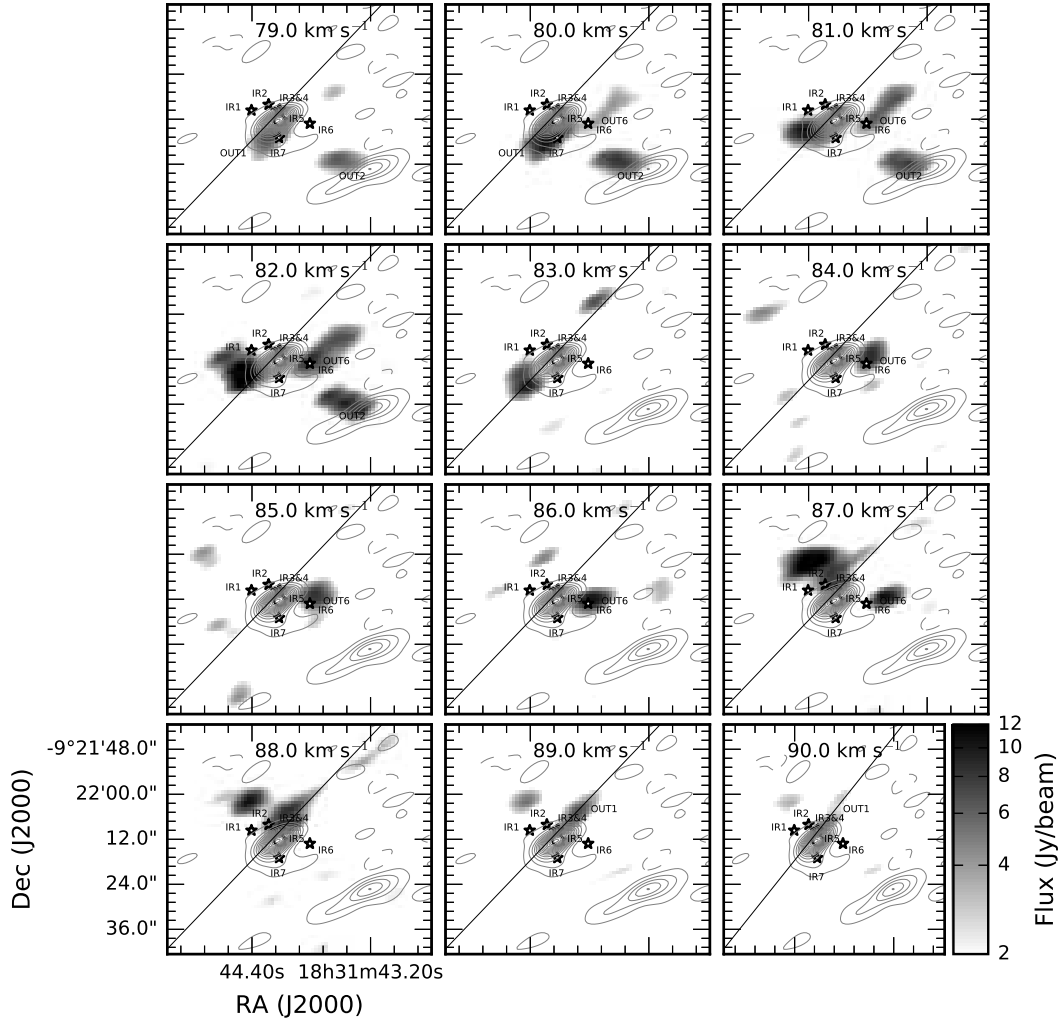
$20 \text{ K}$  with a  $\pm 5 \text{ K}$  uncertainty and used a gas-to-dust mass ratio of 100 to estimate the mass of the cores (MM1 & MM2). The main uncertainty in the estimation of the core mass is from the  $\pm 5 \text{ K}$  uncertainty in the dust temperature and the  $\pm 0.3 \text{ kpc}$  uncertainty in the distance. The mass of the main core (MM1) associated with G22.357+0.066 was estimated to be  $\sim 175 \pm 20 M_\odot$  and for MM2, assuming the same distance as for MM1, the mass was estimated to be  $\sim 52 \pm 6 M_\odot$ .

#### 3.1.2 Carbon-monoxide Emission in G22.357+0.066

Figure 2 presents the channel maps of  $^{12}\text{CO}$  in G22.357+0.066. The dust continuum (white contours) and the near infra-red (NIR 1 to 7) counterparts are superimposed on all the channel maps. The position of the periodic 6.7 GHz methanol maser is indicated by a circle. Using the peak velocity of the  $\text{C}^{18}\text{O}$  line, Szymczak et al. (2007) determined the systemic velocity of G22.357+0.066 to be at  $84.2 \text{ km s}^{-1}$ . The velocity range of the  $^{12}\text{CO}$  is from  $72 \text{ km s}^{-1}$  to  $91 \text{ km s}^{-1}$ , however the channel maps only show the emission from  $79.0 \text{ km s}^{-1}$  to  $90.0 \text{ km s}^{-1}$ . From  $79 \text{ km s}^{-1}$  to  $82 \text{ km s}^{-1}$  there is  $^{12}\text{CO}$  emission (OUT2) associated with MM2 and in channel maps  $80 \text{ km s}^{-1}$  to  $82 \text{ km s}^{-1}$  and  $84 \text{ km s}^{-1}$  to  $87 \text{ km s}^{-1}$ ,  $^{12}\text{CO}$  emission (OUT6) is observed that is associated with the near-infrared source NIR6. In channel map  $79 \text{ km s}^{-1}$  to  $80 \text{ km s}^{-1}$   $^{12}\text{CO}$  emission (OUT1) is observed south-east of the dust continuum MM1 and in channel maps  $89 \text{ km s}^{-1}$  to  $90 \text{ km s}^{-1}$ ,  $^{12}\text{CO}$  emission (OUT1) is observed north-west of MM1. The south-east emission is red-shifted and the north-west emission is blue-shifted. This symmetry (south-east - north-west) seen in the emission with regards to the dust continuum (indicated by the line in Figure 2) is interpreted to be tracing a bipolar outflow as discussed in section 4.1.

**Table 1.** Continuum position parameters

Object-name	R.A. (h m s)	Dec. (° ′ ″)	Peak flux (mJy beam <sup>-1</sup> )	Integrated flux (mJy)	P.A deg
G22.357+0.066 - MM1	18 31 44.15	-09 22 12.6	92.1	94.5	-37.1
G22.357+0.066 - MM2	18 31 43.21	-09 22 25.3	22.6	27.9	
G25.441+0.105 - MM1	18 37 16.94	-06 38 30.1	64.6	66.7	-36.7
G25.441+0.105 - MM2	18 37 16.56	-06 38 32.4	13.7	27.2	
G25.441+0.105 - MM3	18 37 17.18	-06 38 33.4	7.1	13.9	
G9.62+0.19E (MM4)	18 06 14.66	-20 31 31.6	119.1	136.5	81.9

**Figure 2.** G22.357+0.066: <sup>12</sup>CO line emission velocity channel maps from 79.0 km s<sup>-1</sup> to 90.0 km s<sup>-1</sup>.

The position of the periodic methanol maser is indicated with a circle and the grey contours represent the dust continuum with the same contour levels as indicated in the continuum image. The central velocity of each channel is indicated in the upper panel. The NIR counterparts obtained from the UKIDSS database are indicated with the star symbol. The emission is indicated by the grey scale on the bottom right of the channel maps.

### 3.2 G25.411+0.105

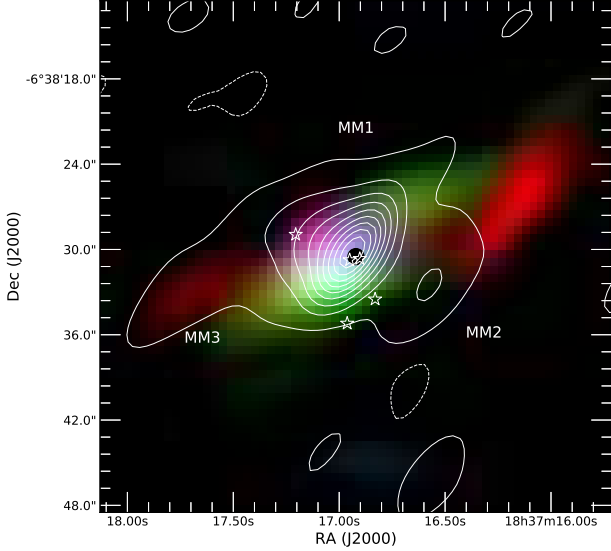
#### 3.2.1 1.3 mm Continuum Emission: G25.411+0.105

Figure 3 shows the millimetre continuum objects (MM1 to MM3) detected in G25.411+0.105, with the rms noise level  $\sim 1$  mJy beam<sup>-1</sup>. Table 1 presents the peak positions (RA and Dec), the peak and integrated flux densities for each de-

tected continuum object. MM2, located west of MM1, has an angular size of  $5''.4 \times 3''.0$  and MM3, located east of MM1, has an angular size of  $6''.3 \times 2''.8$ . Using the methanol multi-beam (MMB) survey position of the masers, the CH<sub>3</sub>OH maser is found to be located  $\sim 0''.22$  from the peak continuum emission (MM1). Using Equation 1 we also adopted a temperature of  $20 \pm 5$  K (Wu et al. 2006; Urquhart et al. 2011;

**Table 2.** Line parameters

Molecule	Transition	Rest frequency (GHz)	$E_L$ (K)
$^{12}\text{CO}$	2-1	230.53800000	5.53
$^{13}\text{CO}$	2-1	220.39868420	5.29
$\text{C}^{18}\text{O}$	2-1	219.56035410	5.27
$\text{CH}_3\text{OH}$	6 <sub>1</sub> -7 <sub>2</sub> A-	217.29920500	363.50



**Figure 3.** G25.411+0.105: 3-color image of the CO emission with the  $^{12}\text{CO}$  in red,  $^{13}\text{CO}$  in green and  $\text{C}^{18}\text{O}$  in blue. The 1.3 mm continuum emission contours are overlaid on the CO emission with the NIR counterparts (star symbol) obtained from UKIDSS Consortium (2012) within a radius of  $5''$  from the maser. MM1 to MM3 indicates each millimetre object detected in the SMA observation. The dust emission contour lines are  $[-2, 2, 10, 18, 26, 34, 42, 50, 58, 66] \times \sigma$  mJy beam $^{-1}$ , with  $\sigma$  as 1 mJy beam $^{-1}$ . The circle shows the position of the periodic 6.7 GHz methanol maser with a  $\sim 6''$  uncertainty.

Lu et al. 2014), since an H II region has not yet been detected in G22.357+0.066 and G25.411+0.105. G25.411+0.105 is located at a distance  $9.5 \pm 0.9$  kpc (Szymczak et al. 2007) and the core mass of G25.411+0.105 (MM1) was estimated to be  $\sim 471 \pm 82 M_\odot$ . The mass for cores MM2 and MM3 were estimated to be  $\sim 192 \pm 42 M_\odot$  and  $98 \pm 16 M_\odot$ , respectively.

### 3.2.2 Carbon-monoxide Emission in G25.411+0.105

The channel maps for the CO emission is not shown for G25.411+0.105 since they all show the same compact emission as seen in the integrated intensity maps, which are indicated by the 3-color image in Figure 3, with red as the  $^{12}\text{CO}$  emission, green the  $^{13}\text{CO}$  emission and the  $\text{C}^{18}\text{O}$  emission is indicated in blue. Unlike the case of G22.357+0.066, most of the CO emissions are spatially distributed around the peak of the dust continuum core (MM1). The  $^{12}\text{CO}$  integrated intensity map shows CO emission associated with MM2 and MM3, west and east of the dust continuum (MM1), respectively and the  $^{13}\text{CO}$  and  $\text{C}^{18}\text{O}$  emission are mostly associated with MM1.

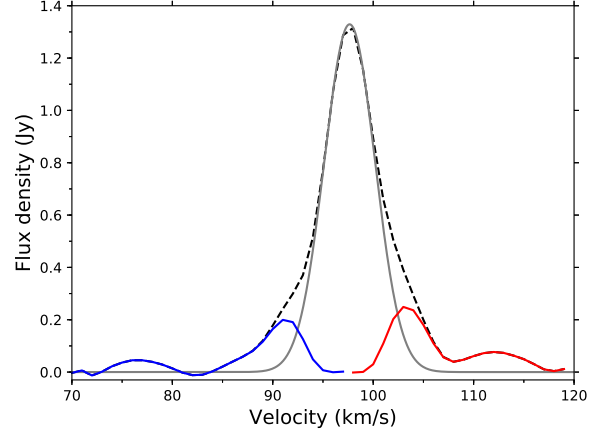


**Figure 4.** G25.411+0.105:  $^{13}\text{CO}$  line spectrum (black), extracted at 80 % flux density from the  $^{13}\text{CO}$  channel maps, with the Gaussian fit (grey). The blue and red lines indicate the blue-shifted and red-shifted emission components (wings).

Figure 4 presents the line spectrum of the  $^{13}\text{CO}$  emission detected towards G25.411+0.105. The Gaussian fit as well as the wing components are indicated on the spectrum. The systemic velocity of G25.411+0.105 is at  $96.0 \text{ km s}^{-1}$  (Szymczak et al. 2007), which was determined by the line peak velocities of  $\text{C}^{34}\text{S}$  (2-1) and  $\text{C}^{34}\text{S}$  (3-2). The blue-shifted ( $85.0 \text{ km s}^{-1}$  to  $95.0 \text{ km s}^{-1}$ ) and red-shifted ( $100.0 \text{ km s}^{-1}$  to  $107.0 \text{ km s}^{-1}$ ) components (wings) are highlighted in blue and red, respectively. The wing channels were extracted as emission associated with out-flowing gas and will be discussed in section 4.1. Szymczak et al. (2007) also found ‘wings’ in the  $^{13}\text{CO}$  spectrum of G25.411+0.105 and they estimated a velocity range of  $11 \text{ km s}^{-1}$  for the  $^{13}\text{CO}$  wings.

## 3.3 G9.62+0.19E

### 3.3.1 1.3 mm Continuum Emission: G9.62+0.19E

Liu et al. (2017) reported 12 millimetre dust continuum cores (MM1 – MM12) for G9.62+0.19 that was detected with ALMA. Our main focus is on the MM4 core (G9.62+0.19E) located at  $(\alpha, \delta)_{\text{J2000.0}} = (18^{\text{h}}06^{\text{m}}14^{\text{s}}.66, -20^{\circ}31'31''.6)$  associated with the periodic methanol masers. Previous observations have reported an ultra-compact H II region and millimetre dust continuum toward G9.62+0.19E e.g. Sanna et al. (2015); Liu et al. (2017); Testi et al. (2000) and Hofner et al. (1996).

Liu et al. (2017) reported the peak intensity of the Gaussian component of the dust emission to be  $0.26 \pm 0.01$  mJy beam $^{-1}$  and the residual point-like component peak intensity to be  $0.93 \pm 0.03$  mJy beam $^{-1}$ . They derived the effective radius of  $1''.65$  corresponding to 8600 au and a core mass of  $74.0 \pm 23.4 M_\odot$  (assuming a dust temperature of 100 K) and a density of  $(4.2 \pm 1.3) \times 10^6 \text{ cm}^{-3}$ . Liu et al. (2017) also detected hot molecular lines such as methyl formate ( $\text{CH}_3\text{OCHO } \nu_t = 1$  (17<sub>4,13</sub>-16<sub>4,12</sub>)) and strong methanol ( $\text{CH}_3\text{OH } \nu_t = 1$ , (6<sub>1</sub>-7<sub>2</sub>)) lines toward G9.62+0.19E, making it a hot core. Liu et al. (2011) derived a rotational temperature of 92 K using six transitions thioformaldehyde ( $\text{H}_2\text{CS}$ ).

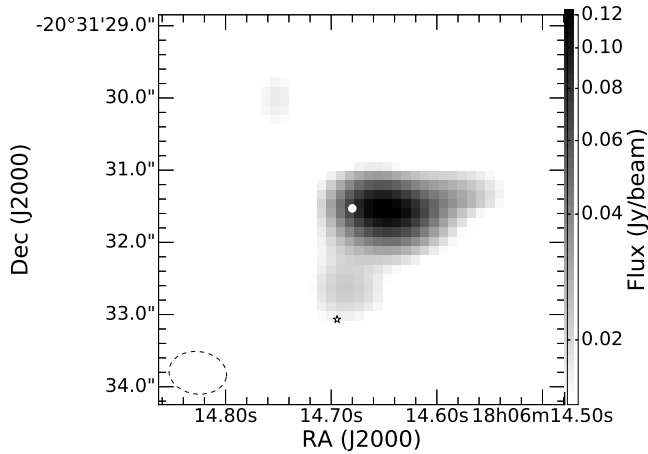


**Figure 5.** G9.62+0.19E: 1.3 mm continuum emission with the NIR counterpart (star symbol) obtained from UKIDSS Consortium (2012) within a radius of 2'' from the maser. The circle shows the position of the periodic 6.7 GHz methanol maser with a  $\sim 6''$  uncertainty. The synthesized beam is shown in the left bottom as an ellipse.

Figure 5 presents the millimetre dust continuum emission of G9.62+0.19E. The methanol maser is marked with a circle and the star symbol indicates the NIR counterpart obtained from the database of the UKIRT Infrared Deep Sky Survey (UKIDSS). Table 1 presents the peak position (RA and Dec) and other continuum parameters G9.62+0.19E (MM4). G9.62+0.19E is located at a distance of  $5.2 \pm 0.6$  kpc (Sanna et al. 2009). Thus from Equation 1 a core mass of  $\sim 59 \pm 14 M_{\odot}$  was estimated for G9.62+0.19E, adopting a dust temperature of  $100 \pm 5$  K, since G9.62+0.19E is a hot core with a H II region (Lu et al. 2014) and Liu et al. (2017) derived a rotational temperature of 92 K for H<sub>2</sub>CS. The uncertainties in the dust temperature and the distance causes the main uncertainty in the core mass.

### 3.3.2 <sup>12</sup>CO Emission in G9.62+0.19E

Unlike our SMA observations, the archival ALMA data of G9.62+0.19E only covers the <sup>12</sup>CO transition and not the <sup>13</sup>CO and C<sup>18</sup>O lines. Figure 6 show the <sup>12</sup>CO channel maps, overlaid is the dust continuum emission (black contours) and the position of the periodic 6.7 GHz methanol maser is indicated by a circle. The systemic velocity of G9.62+0.19E is 2.1 km s<sup>-1</sup> (Liu et al. 2017) determined from the line peak velocity of CH<sub>3</sub>OH  $\nu_t = 1, (6_1-7_2)$ , which makes channel maps -2.7 km s<sup>-1</sup> to 1.0 km s<sup>-1</sup> blue-shifted emission and channel maps 8.0 km s<sup>-1</sup> to 10.7 km s<sup>-1</sup> red-shifted emission. Figure 6 shows an emission core north-west of the dust continuum at -2.7 km s<sup>-1</sup>, the core peaks at -0.4 km s<sup>-1</sup> and disappears after 0.3 km s<sup>-1</sup>. A second blue-shifted emission core appears at -0.4 km s<sup>-1</sup> on the dust continuum and extend to the south-east of the dust continuum, after which it disappears at 0.6 km s<sup>-1</sup>. Figure 6 shows two red-shifted emission cores that appear at 8.0 km s<sup>-1</sup>. One core is located north-west of the dust continuum and the other is south-east of the dust continuum. The south-east core disappears after 9.7 km s<sup>-1</sup> and the north-west core peaks at 10.1 km s<sup>-1</sup>, after which it disappears at 10.7 km s<sup>-1</sup>. Thus there are two blue-shifted

emission cores and two red-shifted emission cores found in the <sup>12</sup>CO emission, which indicates to evidence of a north-west - south-east multi-bipolar outflow system and will be discussed in section 4.1.

### 3.3.3 Rotation in the methanol of G9.62+0.19E

Figure 8 shows the CH<sub>3</sub>OH  $\nu_t = 1, (6_1-7_2)$  detected towards G9.62+0.19E. The CH<sub>3</sub>OH emission has a compact morphology on the dust continuum and Liu et al. (2017) fitted the CH<sub>3</sub>OH spectrum with a Gaussian profile and obtained a FWHM of  $4.70 \pm 0.02$  km s<sup>-1</sup>. The methanol data was explored further in search for rotation, since it might lead to a better understanding of the multi-outflow system observed in the <sup>12</sup>CO velocity channel maps. Figure 8 is the velocity field map (moment 1 map) of CH<sub>3</sub>OH  $\nu_t = 1, (6_1-7_2 A-)$  obtained from the data of Liu et al. (2017) and shows a spatial separation of the red- and blue-shifted emission, indicating evidence of rotational motion with the enclosed mass being  $\sim 70\%$  of the core mass. These velocity gradients in the methanol moment 1 map that suggests rotation were also reported by Liu et al. (2017). In addition, Liu et al. (2011) (their Fig. 4) also reported rotation associated with G9.62+0.19E using the H<sub>2</sub>CS (10<sub>2,8</sub> - 9<sub>2,7</sub>) line. The red and blue contours superimposed on the methanol were obtained from the peak intensities of the blue- and red-shifted emission in the <sup>12</sup>CO (Figure 7 and the line indicates the general orientation of the bipolar outflows). VLBI observations toward G9.62+0.19E by Sanna et al. (2015) revealed two continuum cores within core E and are indicated as sub-continuum cores E1 and E2.

## 4 DISCUSSION

### 4.1 Disk-outflow orientation

The <sup>12</sup>CO velocity channel maps of G9.62+0.19E (Figure 6) show a clear north-west - south-east multi-outflow structure. The case of G9.62+0.19E is not as simple and requires further consideration. Although Sanna et al. (2015) identified a second sub-continuum source (E2) offset in projection by 1300 AU from sub-continuum core E1 in G9.62+0.19E, the periodic masers are clearly associated with core E1 as is seen from Figure 1 of Sanna et al. (2015). This applies also to the periodic OH masers associated with this region as argued by Goedhart et al. (2019). The exact relation between components E1 and E2 is not clear even though both of these are projected inside the core as is evidenced in Figure 8. The axis of the outflow suggest that it is driven by the YSO associated with E1. However, the angular resolution of our data is not sufficient to confirm whether some of the outflowing gas emanate from E2. Considering the velocity field map (Figure 8) of G9.62+0.19E, the velocity gradient seen in the CH<sub>3</sub>OH  $\nu_t = 1, (6_1-7_2 A-)$  points to a disk with an inclination along the line of sight.

The symmetry (south-east and north-west emission) seen in the <sup>12</sup>CO channel maps (Figure 2) of G22.357+0.066 shows evidence of outflow from a central core (MM1). The emission south-east and north-west of G22.357+0.066-MM1 was extracted and imaged as red- and blue-shifted emission and is presented in Figure 9 as a bipolar outflow. The <sup>12</sup>CO emission

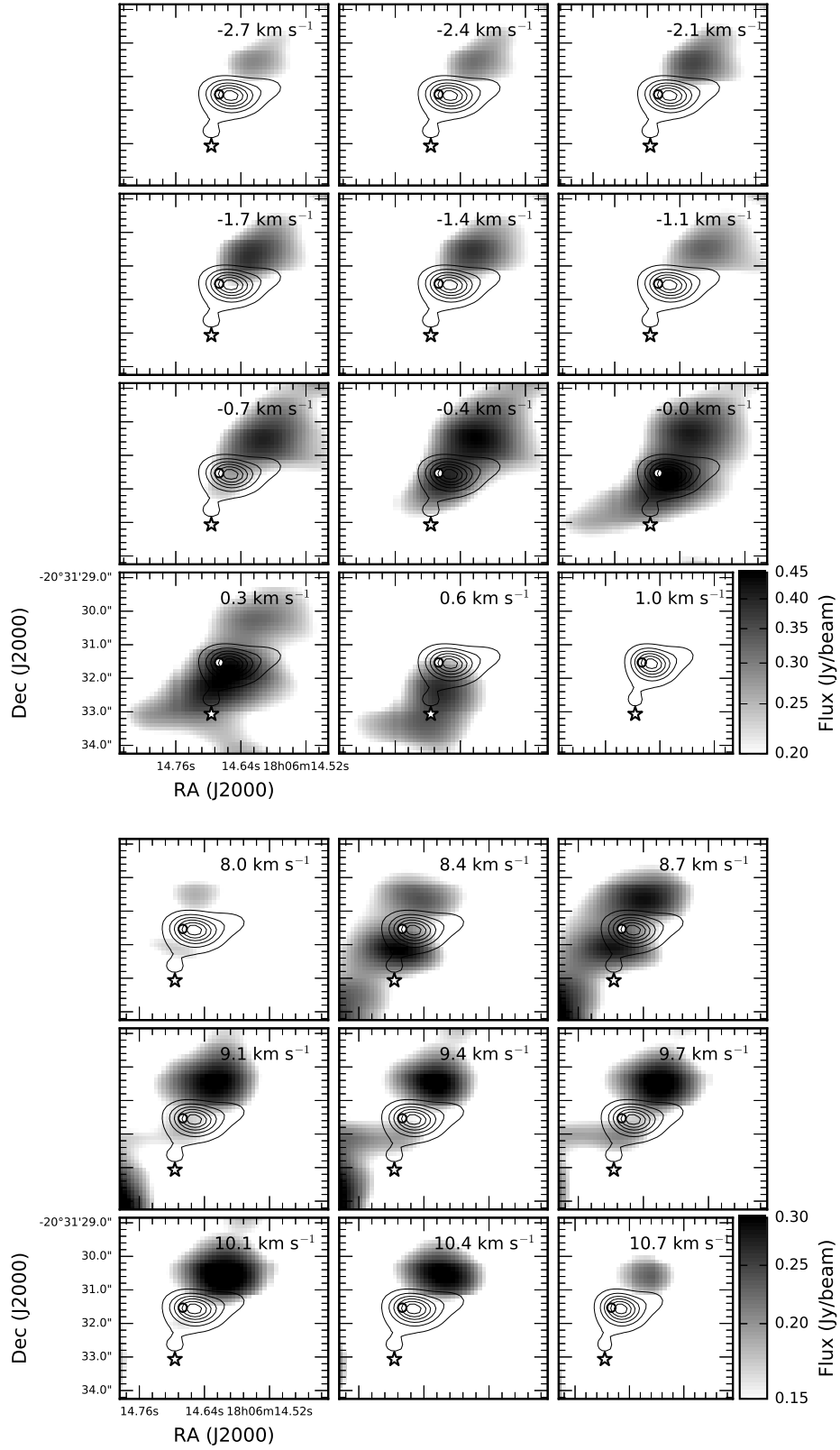


**Figure 6.** G9.62+0.19E:  $^{12}\text{CO}$  blue-shifted velocity channel maps from  $-2.7 \text{ km s}^{-1}$  to  $1.0 \text{ km s}^{-1}$  and the red-shifted velocity channel maps from  $8.0 \text{ km s}^{-1}$  to  $10.7 \text{ km s}^{-1}$ . The position of the periodic methanol maser is indicated with a circle and the dust continuum contours levels are  $[20, 40, 60, 80, 100, 120, 140] \times \sigma \text{ mJy beam}^{-1}$ , where  $\sigma$  is  $1 \text{ mJy beam}^{-1}$ . The NIR counterpart obtained from the UKIDSS database is indicated with the star symbol.

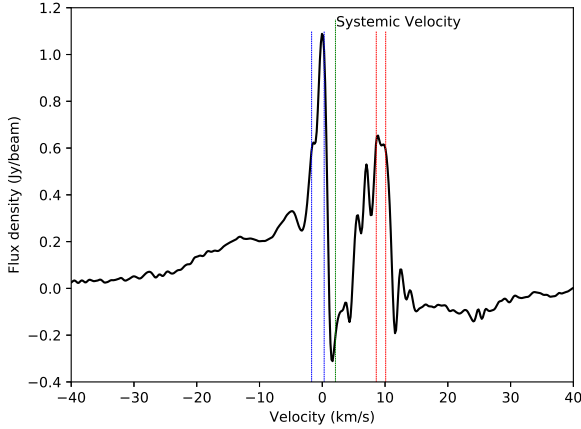


**Figure 7.**  $^{12}\text{CO}$  spectrum of G9.62+0.19E. The systemic velocity ( $2.1 \text{ km s}^{-1}$ ) is indicated in green and the peak intensities of the blue- and red-shifted cores are indicated in blue ( $-1.7 \text{ km s}^{-1}$  and  $0.3 \text{ km s}^{-1}$ ) and red ( $8.3 \text{ km s}^{-1}$  and  $10.1 \text{ km s}^{-1}$ ), respectively

in G22.357+0.066 is quite complex, but channels  $79 \text{ km s}^{-1}$  to  $80 \text{ km s}^{-1}$  and  $89 \text{ km s}^{-1}$  to  $90 \text{ km s}^{-1}$  of  $^{12}\text{CO}$  (Figure 2), indicate bipolarity in their symmetry which cut through the peak position of G22.357+0.066-MM1

The  $^{13}\text{CO}$  spectrum (Figure 4) of G25.411+0.105 shows wings, which is interpreted as outflow from a central core. The  $^{13}\text{CO}$  channels falling in the velocity ranges of the blue and red-shifted components were extracted and imaged as blue- and red-shifted emission. Figure 10 present the bipolar outflow of G25.411+0.105. The red- and blue-shifted components of the outflow are spatially coincident, which indicates that the outflow direction is along the line of sight of the observer. Assuming a disk-outflow system, then the rotating structure around G25.411+0.105 must be face-on with the axis of rotation closely aligned with the line of sight.

The inclination angle (relative to the line-of-sight) in G9.62+0.19E and G22.357+0.066 was calculated using the method given in Kong & Wu (2011). For G22.357+0.066 the maser position was chosen as the center of the driving source and a inclination angle of  $\sim 82^\circ$  was obtained. For G9.62+0.19E two driving source positions were chosen, the maser and core E1. The inclination angle obtained using the maser is  $\sim 82^\circ$  and the inclination angle found using E1 as the position is the driving source is  $\sim 57^\circ$ . The orientation (inclination angles) of the bipolar outflow of G9.62+0.19E ( $\sim 71^\circ$ ) and G22.357+0.066  $\sim 82^\circ$  are similar to one another, but different from the outflow orientation of G25.411+0.105. In the case of G22.357+0.066 and G9.62+0.19E the bipolar outflows are almost in the plane (inclination of  $\sim 82^\circ$  and  $\sim 71^\circ$ , respectively) of the sky. The method used in Kong & Wu (2011) can not be applied to G25.411+0.105 to obtain a inclination angle, since it can only be used for a conical-like outflow. The presence of bipolar outflows also imply the existence of disks (Cesaroni et al. 2007). Thus, since G22.357+0.066 and G9.62+0.19E have outflows orientated almost in the plane of the sky, their disks would be viewed approximately edge-on with some inclination. For G25.411+0.105 which has an outflow orientated almost perpendicular to the plane of the sky, the disk would then be viewed face-on.

From Figure 11, it can be seen that the periodic methanol masers of G9.62+0.19E and G22.357+0.066 have similar light curves and they also have similar outflow orientations (Figures 8 and 9). Based on the presence of an H II region in G9.62+0.19E and the non-detection thereof in G22.357+0.066 by (Bartkiewicz et al. 2011), G9.62+0.19E is likely to be more evolved than G22.357+0.066. Figure 11 also shows that G25.411+0.105 has a different periodic methanol maser light curve from that of G9.62+0.19E and G22.357+0.066 and has a different outflow orientation (Figure 10). This may point to inclination and/or orientation effects as a possible cause of the difference in the flare profiles of the periodic methanol maser considered here.

#### 4.2 Possible Explanations of the Impact of Source Orientation

Although the results presented above are for only three sources, it nevertheless is rather remarkable that for G9.62+0.19E and G22.357+0.066, which have similar light curves and which can be explained within the framework of the CWB scenario, the observations suggest that the outflows associated with each of the sources are projected almost in the plane of the sky. On the other hand, G25.411+0.105, with a completely different periodic maser light curve (bunny hop), seems to have an orientation such that the associated outflow is almost perpendicular to the plane of the sky. The question is how and whether such differences in the orientation of the source can play a role in determining the shape of the light curve of the periodic masers.

It is not yet clear where in the environment of the young high-mass stars the methanol masers arise. However, van der Walt et al. (2016) argued that the shape of the maser light curve reflects the underlying mechanism that gives rise to the periodicity. Implicitly this means that the masing region's position and orientation must be such that the variation in the maser emission reflects the effects of the underlying mechanism of the periodicity. For G9.62+0.19E and G22.357+0.066 the implication within the CWB scenario is that the periodic masers must be projected against an H II region. Given the observational results for the three periodic masers, we argue here that the difference in the light curves of G9.62+0.19E and G22.357+0.066 on the one hand and G25.411+0.105 on the other hand may be due to the masers in these three sources being located in accretion disks or rotating toroidal structures but have different orientations in these structures. By making this assumption we do not exclude other possibilities for where the masers may arise (eg. from outflowing gas) but apply it only to the current discussion.

The scenario we propose is a combination of an inner disk as that shown in Fig. 6 of Vaidya et al. (2009) and a rotating torus as in Fig. 9 of Sollins et al. (2005) with the inner disk being feeded with material from the rotating torus. Comparison of Fig. 8 with the equivalent maps of G10.62-0.38, G19.61-0.23 and G29.96-0.02 (Beltrán et al. 2011) suggests that a rotating toroid is also present in G9.62+0.19E. Associated with the disk-torus system is a bipolar outflow which carved out a conical shaped cavity in the central part of the torus. Depending on the evolutionary state of the high-mass star, a small H II region may be present similar to that proposed by Sollins et al. (2005) for G28.20-0.05. The H II re-

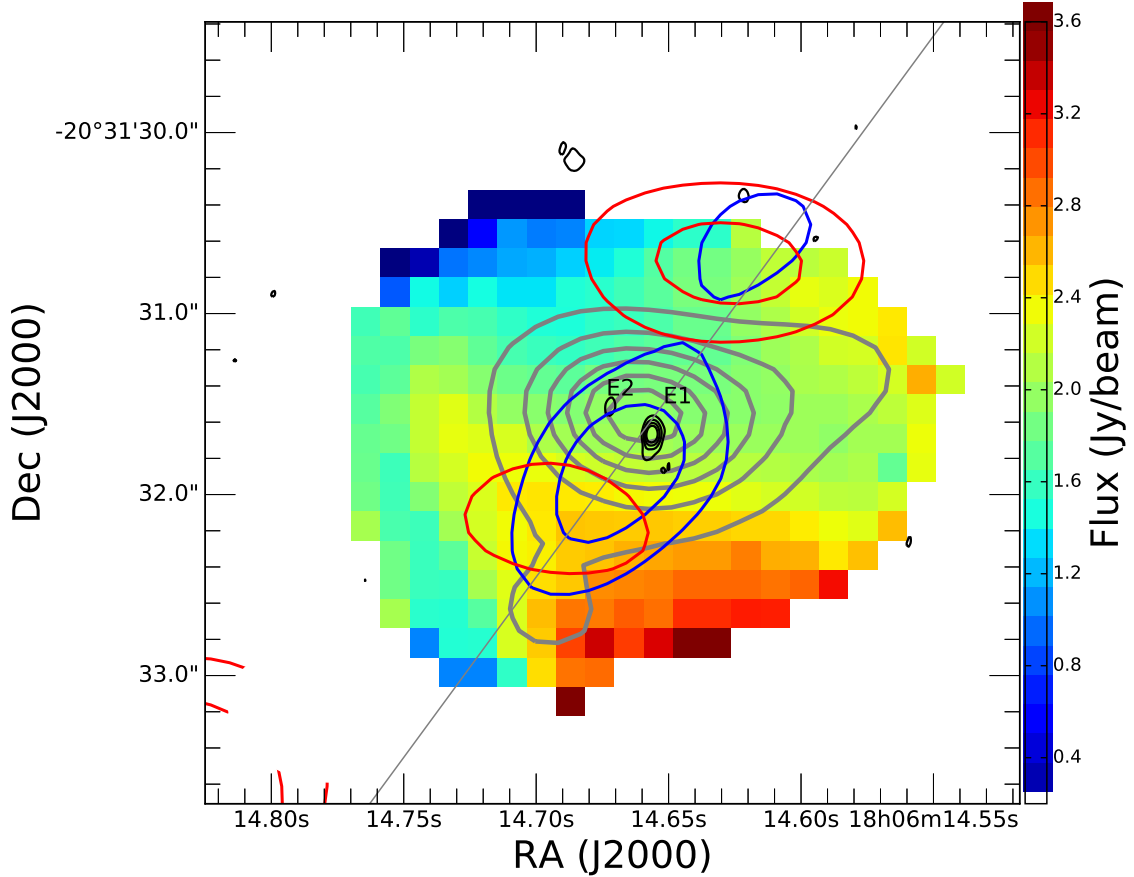


**Figure 8.** Moment 1 map of CH<sub>3</sub>OH  $v_t = 1$ , (6<sub>1</sub>-7<sub>2</sub> A-) emission of G9.62+0.19E obtained from Liu et al. (2017). The dark grey solid contour lines is the dust continuum and has the same levels as indicated in Figure 5. The blue and red contours indicate the peak intensities of the blue- and red-shifted emission as seen in the <sup>12</sup>CO line spectrum (Figure 7). E1 and E2 represents the sub-continuum cores detected by Sanna et al. (2015) with the contour levels [1.0, 2.0, 3.0, 4.0] mJy beam<sup>-1</sup>. The grey line indicates the direction of the bipolar outflow in G9.62+0.19E.

gion may be a trapped H II region (Keto 2002) or it may already have expanded into the lower density cavity created by the outflow as suggested in Fig. 9 of Sartorio et al. (2019). For the masers we consider two cases for the orientation of the masing columns, ie. perpendicular to the plane of the disk-torus system or in the plane of the disk-torus system. The assumption that the masers are located in a disk is not new. Parfenov & Sobolev (2014) made a similar assumption in their model. A schematic representation of this scenario is shown in Fig. 12.

Consider first the edge-on view as seen from the vantage point of observer B as shown in Fig. 12. It is quite obvious that masers in the plane of the disk/torus can indeed be projected against the H II region and that the CWB scenario is in agreement with such a geometry. Given that the maser flare profiles of G9.62+0.19E and G22.357+0.066 can be explained within the CWB scenario, and that the observed outflows for these two sources are projected almost in the plane of the sky, suggest that the geometry as for observer B in Fig. 12 might apply to these two sources. Depending on the physical conditions in the disk/torus, it is possible that some masers in the plane of the disk/torus might not be projected directly against the H II region. However, the possibility of not being projected against the H II region is not as severe as in the

case for masers oriented perpendicular to the plane of the disk/torus as discussed next.

Thus, consider the case in which the disk-torus is viewed face-on, ie. from the position of observer A in Fig. 12. This scenario will correspond to that of G25.411+0.105, viz. where the observed outflow is almost perpendicular to the plane of the sky. The effect of the outflow and the cavity it creates is that masers located in the disk and which are pointing towards the observer cannot be projected against the H II region. Also, due to the radial dependence of the density and temperature in the disk/torus it is reasonable to assume that the masers will arise at those radial positions where the conditions for pumping are optimal. According to Cragg et al. (2002) the conditions under which class II methanol masers are pumped are for  $n_{H_2} < 10^8$  cm<sup>-3</sup>, and  $T_k < T_d \simeq 175$ K with  $T_k$  the gas kinetic temperature and  $T_d$  the dust temperature. Parfenov & Sobolev (2014) set the upper limit for the density at  $n_{H_2} = 10^9$  cm<sup>-3</sup> and a dust temperature > 100 K. Using these numbers with the theoretical results of Kuiper & Yorke (2013), it is found that the masers can occur at distances greater than about 400 AU from the star provided that  $T_d > 100$ K. There is therefore at least two physically justifiable reasons why in the case of this geometry the

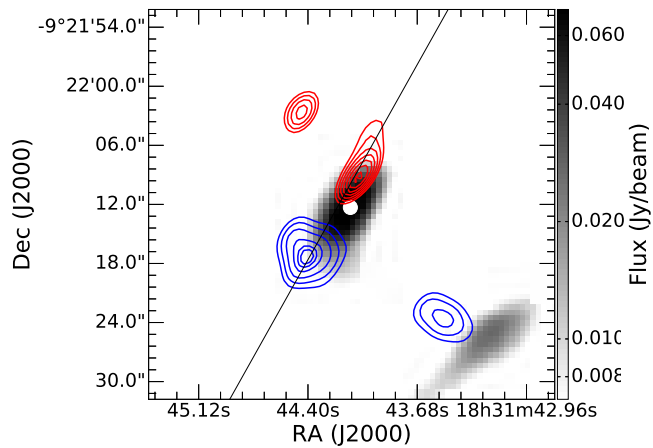


**Figure 9.** Bipolar outflow of G22.357+0.066 traced by the  $^{12}$ CO emission. The red and blue contours that indicate the blue-shifted ( $72 \text{ km s}^{-1} \sim 80 \text{ km s}^{-1}$ ) and red-shifted ( $88 \text{ km s}^{-1} \sim 92 \text{ km s}^{-1}$ ) emission respectively are superimposed on the dust continuum. The black line indicates the direction of the bipolar outflow. The circle is the periodic methanol maser.

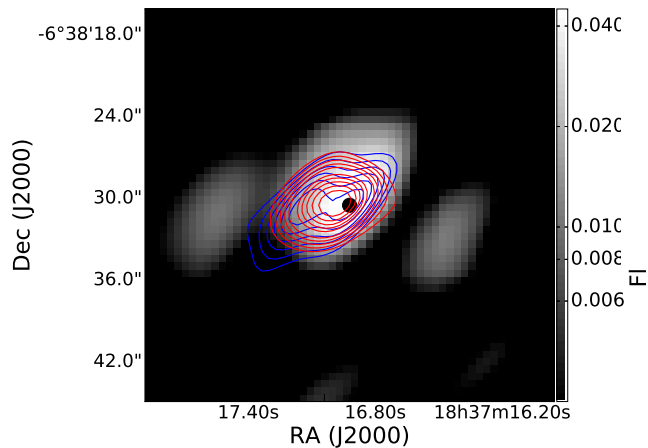
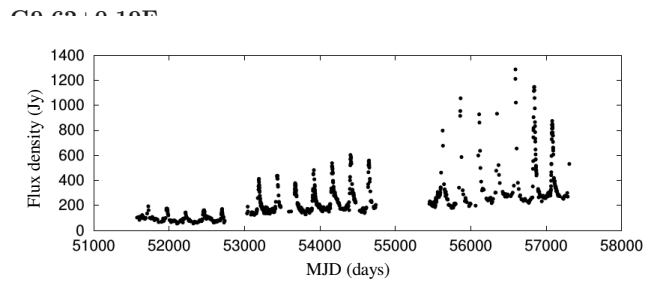


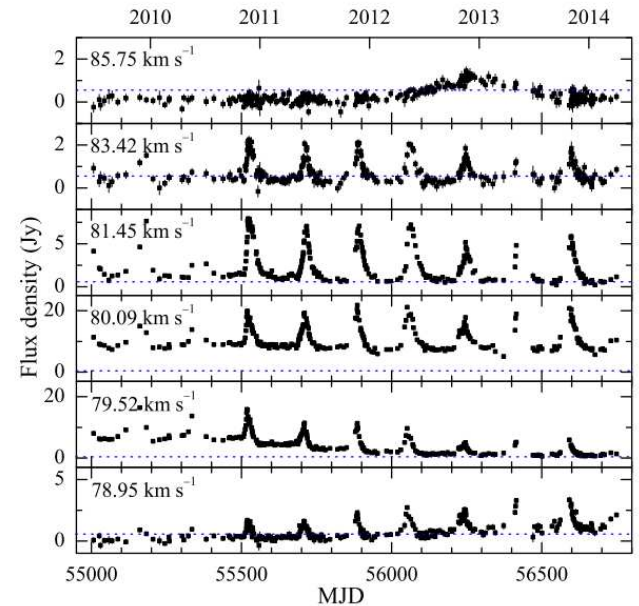
**Figure 10.** Bipolar outflow of G25.411+0.105 traced by the  $^{13}$ CO emission. The red and blue contours indicate the blue-shifted ( $89 \text{ km s}^{-1} \sim 91 \text{ km s}^{-1}$ ) and red-shifted ( $102 \text{ km s}^{-1} \sim 104 \text{ km s}^{-1}$ ) emission respectively that are superimposed on the dust continuum. The circle is the periodic methanol maser.

masers cannot be projected against the H II region if they are located in the disk/torus.

From these considerations it follows that the orientation of the disk/torus-outflow system in the sky does play a role in “selecting” which scenarios for the periodic variability of methanol masers are compatible with a particular flare profile. For example, for the CWB scenario (van der Walt 2011; van den Heever et al. 2019), in which the decay of the maser follows that of a recombining partially ionized hydrogen plasma, it is required that the masers be projected against some part of the H II region and is therefore not compatible with a face-on orientation of the disk/torus. If in fact the face-on case implies that the periodic masers are not projected against an H II region, it follows that the underlying cause for the periodicity is most likely related to a process that periodically changes the physical conditions



**G22.357+0.066**



**G25.411+0.105**

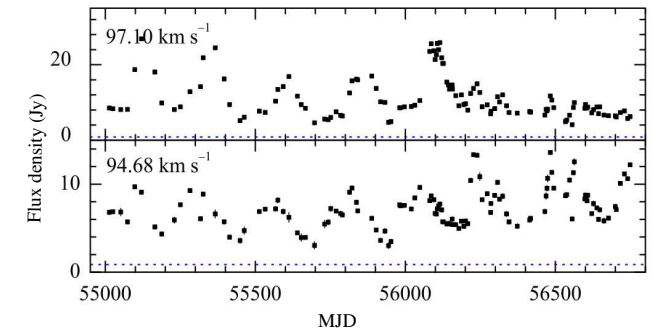


**Figure 11.** Light curve profiles of G9.62+0.19E obtained from (Goedhart et al. 2014), G22.357+0.066 and G25.411+0.105, both obtained from (Szymczak et al. 2015).

in the masing region or in its immediate vicinity. It might, therefore, be that in this case the proposed models of eg. Araya et al. (2010) and Parfenov & Sobolev (2014) are applicable. It should be noted that in the models of Araya et al. (2010) and Parfenov & Sobolev (2014) the proposed binary system might also be a CWB but its effect on the masers will definitely be different than for the case when the masers are projected against the H II region and the variability is not due to changes in the free-free seed photon flux.

In the case of G25.411+0.105, for which an outflow almost along the line-of-sight has been detected, a ring-like distribu-

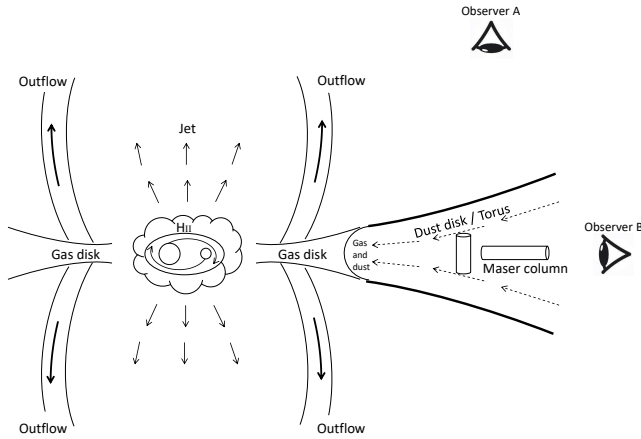


**Figure 12.** Schematic to illustrate the effect of different orientations of the masing columns of gas. Adapted from Vaidya et al. (2009).

tion of masers has been mapped by Bartkiewicz et al. (2009). These authors fitted an ellipse to the distribution of masers, suggesting that the disk is not viewed perfectly face-on which is in agreement with the observation that the outflow axis is somewhat inclined relative to the line-of-sight. At a distance of 9.5 kpc the linear radius of the ring distribution is 980 AU (Bartkiewicz et al. 2009) which agrees with the above rough estimate that the conditions for class II methanol masers occur at radial distances greater than 400 AU. Szymczak et al. (2015) presented the time series of the maser features at  $94.6 \text{ km s}^{-1}$  and  $97.1 \text{ km s}^{-1}$  of G25.411+0.105. A comparison of the two time series suggests that the feature at  $94.6 \text{ km s}^{-1}$  reaches a maximum about 30 days before the feature at  $97.1 \text{ km s}^{-1}$ . Using the elliptical fit of Bartkiewicz et al. (2009) and the positions of these two features, it is found that, in projection, the angle between the two features is about  $42^\circ$ . Assuming the presence of a binary system then, for an orbital period of 245 days, such an angular separation translates to a delay of 28.6 days, which is surprisingly similar to the time lag in the observed time series of these two maser features. Although it is not possible to explain the shape of the light curves for the periodic masers, it would seem that there is real evidence for a binary system viewed face-on.

We also searched the literature for other imaging observations done on periodic methanol maser sources with light curves similar to that of G9.62+0.19E or those with bunny-hop type light curves. Li et al. (2016) mapped a  $^{12}\text{CO}(1-0)$  outflow associated with the periodic methanol maser source G45.473+0.133 which have a maser light curve similar to that of G9.62+0.19E. The period of the maser is 195.7 days (Szymczak et al. 2015). The red- and blue-shifted lobes are clearly separated even with a beam of  $52''$ . Although it is not possible to determine the exact orientation, these observations show that the outflow axis is most likely closer to the plane of the sky than perpendicular to it. More detailed observations of this source is required to come to a conclusion about the orientation of the outflow axis. It nevertheless seems as if there is evidence that G45.473+0.133 shares the same properties as G9.62+0.19E and G22.357+0.066, ie. a periodic maser light curve that resembles that of G9.62+0.19E

with an outflow perpendicular or nearly perpendicular to the line of sight.

One consequence of the above described scenario is that in the case of the masers located in a disk/torus being viewed face-on, the maser velocities must be close to the systemic velocity and/or have a rather small velocity range. Apart from G25.411+0.105 there are two more periodic maser sources for which the light curves has the bunny-hop behaviour, ie. G338.93-0.06 (Goedhart et al. 2014) and G358.460-0.391 (Maswanganye et al. 2015). In the case of G25.411+0.105, the systemic velocity from the Gaussian fit in Fig. 4 is  $97.5 \text{ km s}^{-1}$ . Szymczak et al. (2015) report two maser features respectively at  $94.68$  and  $97.1 \text{ km s}^{-1}$ . Both maser features lie within about  $2.8 \text{ km s}^{-1}$  from the systemic velocity. Using the systemic velocity of  $96.0 \text{ km s}^{-1}$  of Szymczak et al. (2007), the offset is at most  $1.3 \text{ km s}^{-1}$ . Goedhart et al. (2014) reported two maser features at  $-42.183$  and  $-41.376 \text{ km s}^{-1}$  for G338.93-0.06, thus a velocity range of only  $\sim 0.8 \text{ km s}^{-1}$ . The systemic velocity is taken as  $-44.3 \text{ km s}^{-1}$  from the MALT90 survey (Rathborne et al. 2016). The offset from the systemic velocity is therefor less than  $2.1 \text{ km s}^{-1}$ . In the case of G358.460-0.391 no thermal line emission spectrum could be found to determine the systemic velocity. However, the maser spectrum shows only two maser features that differ in velocity with less than  $1 \text{ km s}^{-1}$  (Maswanganye et al. 2015).

For G9.62+0.19E, G22.357+0.066 and G45.473+0.133 we note the following. The velocity range for the masers in G9.62+0.19E is at least  $7.6 \text{ km s}^{-1}$  (Goedhart et al. 2014),  $4.47 \text{ km s}^{-1}$  for G22.357+0.066 and  $\sim 8 \text{ km s}^{-1}$  for G45.473+0.133 (Szymczak et al. 2015). In the case of G22.357 all the periodic masers are blue shifted with respect to the systemic velocity of  $84.2 \text{ km s}^{-1}$ , with the largest velocity offset being  $5.3 \text{ km s}^{-1}$ . The systemic velocity of G45.473+0.133 of  $63.1 \text{ km s}^{-1}$  (Szymczak et al. 2015) implies that the largest maser velocity offset from the systemic velocity is about  $10 \text{ km s}^{-1}$ . In the case of G9.62+0.19E the systemic velocity is at  $1.9 \text{ km s}^{-1}$  with the blue shifted periodic masers being offset by up to  $2.4 \text{ km s}^{-1}$  and the red shifted masers up to  $4.5 \text{ km s}^{-1}$  from the systemic velocity.

It is rather remarkable that the three sources which have periodic maser light curves that can be explained within the framework of a CWB scenario have similar properties. The same applies to the three sources for which the light curves have a bunny-hop shape, even though we have mapped only G25.411+0.105.

## 5 CONCLUSIONS

We observed two periodic methanol maser sources, ie. G22.357+0.066 and G25.411+0.105 with the SMA and used archival ALMA data for G9.62+0.19E to investigate whether there are larger scale differences between the three high-mass star forming regions that might explain the difference in the maser light curves. The periodic masers in G9.62+0.19E and G22.357-0.066 have the same type of light curve while for G25.411+0.105 the light curve resembles a  $|\cos(\omega t)|$  function, also referred to as a bunny-hop.

The observations indicated that both G9.62+0.19E and G22.357+0.066 have outflows which are aligned close to the plane of the sky. In the case of G25.411+0.105 an outflow aligned close to the line of sight was detected. While no di-

rect detection of accretion disks was possible with the current observations, the detected outflows suggest the presence of accretion disks in all three these systems. Considering the orientation of the outflows, our observations suggest that the accretion disks or rotating toroidal structures in G9.62+0.19E and G22.357+0.066 are viewed edge-on and face-on in the case of G25.411+0.105. Together with the inferences from the maser spectra and systemic velocities of G45.473+0.133, G339.93−0.06, and G358.460−0.391, it is concluded that orientation effects may play a role in determining the characteristics of the light curves of periodic methanol masers.

## ACKNOWLEDGEMENTS

We thank Dr. Liu Tie and Dr. Alberto Sanna for providing us with the ALMA and VLA fits images of G9.62+0.19E, respectively. This paper makes use of the following ALMA data: ADS/JAO.ALMA#2013.1.00957.S. ALMA is a partnership of ESO (representing its member states), NSF (USA) and NINS (Japan), together with NRC (Canada), MOST and ASIAA (Taiwan), and KASI (Republic of Korea), in cooperation with the Republic of Chile. The Joint ALMA Observatory is operated by ESO, AUI/NRAO and NAOJ. JvdW acknowledge support by the National Research Foundation of South Africa (NRF Grant Number 132494). JM and JOC acknowledge support by the Italian Ministry of Foreign Affairs and International Cooperation (MAECI Grant Number ZA18GR02) and the South African Department of Science and Technology's National Research Foundation (DST-NRF Grant Number 113121) as part of the ISARP RADIOSKY2020 Joint Research Scheme.

## DATA AVAILABILITY

The data used in producing the results in this article can be accessed from Submillimeter Array (SMA) and the Atacama Large Millimeter/submillimeter Array (ALMA). The raw data sets can be download from the SMA and ALMA archives.

## REFERENCES

Araya E. D., Hofner P., Goss W. M., Kurtz S., Richards A. M. S., Linz H., Olmi L., Sewilo M., 2010, *ApJ*, **717**, L133  
 Bartkiewicz A., Szymczak M., van Langevelde H. J., Richards A. M. S., Pihlström Y. M., 2009, *A&A*, **502**, 155  
 Bartkiewicz A., Szymczak M., Pihlström Y. M., van Langevelde H. J., Brunthaler A., Reid M. J., 2011, *A&A*, **525**, A120  
 Beltrán M. T., Cesaroni R., Neri R., Codella C., 2011, *A&A*, **525**, A151  
 Breen S. L., Ellingsen S. P., Contreras Y., Green J. A., Caswell J. L., Stevens J. B., Dawson J. R., Voronkov M. A., 2013, *MNRAS*, **435**, 524  
 Cesaroni R., Galli D., Lodato G., Walmsley C. M., Zhang Q., 2007, *Protostars and Planets V*, pp 197–212  
 Cragg D. M., Sobolev A. M., Godfrey P. D., 2002, *MNRAS*, **331**, 521  
 Goedhart S., Gaylard M. J., van der Walt D. J., 2003, *MNRAS*, **339**, L33  
 Goedhart S., Gaylard M. J., van der Walt D. J., 2004, *MNRAS*, **355**, 553

Goedhart S., Maswanganye J. P., Gaylard M. J., van der Walt D. J., 2014, *MNRAS*, **437**, 1808  
 Goedhart S., van Rooyen R., van der Walt D. J., Maswanganye J. P., Sanna A., MacLeod G. C., van den Heever S. P., 2019, *MNRAS*, **485**, 4676  
 Hildebrand R. H., 1983, *QJRAS*, **24**, 267  
 Hirota T., Machida M. N., Matsushita Y., Motogi K., Matsumoto N., Kim M. K., Burns R. A., Honma M., 2017, *Nature Astronomy*, **1**, 0146  
 Hofner P., Kurtz S., Churchwell E., Walmsley C. M., Cesaroni R., 1996, *ApJ*, **460**, 359  
 Ilee J. D., Cyganowski C. J., Nazari P., Hunter T. R., Brogan C. L., Forgan D. H., Zhang Q., 2016, *MNRAS*, **462**, 4386  
 Inayoshi K., Sugiyama K., Hosokawa T., Motogi K., Tanaka K. E. I., 2013, *ApJ*, **769**, L20  
 Keto E., 2002, *ApJ*, **568**, 754  
 Kong S., Wu Y., 2011, *MNRAS*, **413**, 71  
 Kuiper R., Yorke H. W., 2013, *ApJ*, **763**, 104  
 Li F. C., Xu Y., Wu Y. W., Yang J., Lu D. R., Menten K. M., Henkel C., 2016, *AJ*, **152**, 92  
 Liu T., Wu Y., Liu S.-Y., Qin S.-L., Su Y.-N., Chen H.-R., Ren Z., 2011, *ApJ*, **730**, 102  
 Liu T., et al., 2017, *ApJ*, **849**, 25  
 Lu X., Zhang Q., Liu H. B., Wang J., Gu Q., 2014, *ApJ*, **790**, 84  
 Maswanganye J. P., Gaylard M. J., Goedhart S., Walt D. J. v. d., Booth R. S., 2015, *MNRAS*, **446**, 2730  
 Parfenov S. Y., Sobolev A. M., 2014, *MNRAS*, **444**, 620  
 Rathborne J. M., et al., 2016, *Publ. Astron. Soc. Australia*, **33**, e030  
 Reid M. J., et al., 2009, *ApJ*, **700**, 137  
 Sanna A., Reid M. J., Moscadelli L., Dame T. M., Menten K. M., Brunthaler A., Zheng X. W., Xu Y., 2009, *ApJ*, **706**, 464  
 Sanna A., et al., 2015, *ApJ*, **804**, L2  
 Sartorio N. S., Vandenbroucke B., Falceta-Goncalves D., Wood K., Keto E., 2019, *MNRAS*, **486**, 5171  
 Singh N. K., Deshpande A. A., 2012, in Booth R. S., Vlemmings W. H. T., Humphreys E. M. L., eds, *IAU Symposium Vol. 287, Cosmic Masers - from OH to H0*. pp 93–97 ([arXiv:1203.3427](https://arxiv.org/abs/1203.3427)), doi:10.1017/S1743921312006710  
 Sollins P. K., Zhang Q., Keto E., Ho P. T. P., 2005, *ApJ*, **631**, 399  
 Sridharan T. K., Beuther H., Schilke P., Menten K. M., Wyrowski F., 2002, *ApJ*, **566**, 931  
 Szymczak M., Bartkiewicz A., Richards A. M. S., 2007, *A&A*, **468**, 617  
 Szymczak M., Wolak P., Bartkiewicz A., van Langevelde H. J., 2011, *A&A*, **531**, L3  
 Szymczak M., Wolak P., Bartkiewicz A., 2015, *MNRAS*, **448**, 2284  
 Testi L., Hofner P., Kurtz S., Rupen M., 2000, *A&A*, **359**, L5  
 UKIDSS Consortium 2012, *VizieR Online Data Catalog*, **2316**  
 Urquhart J. S., et al., 2011, *MNRAS*, **418**, 1689  
 Vaidya B., Fendt C., Beuther H., 2009, *ApJ*, **702**, 567  
 Weingartner J. C., Draine B. T., 2001, *ApJ*, **548**, 296  
 Wu Y., Zhang Q., Yu W., Miller M., Mao R., Sun K., Wang Y., 2006, *A&A*, **450**, 607  
 van den Heever S. P., van der Walt D. J., Pittard J. M., Hoare M. G., 2019, *MNRAS*, **485**, 2759  
 van der Walt D. J., 2011, *AJ*, **141**, 152  
 van der Walt D. J., Goedhart S., Gaylard M. J., 2009, *MNRAS*, **398**, 961  
 van der Walt D. J., Maswanganye J. P., Etoke S., Goedhart S., van den Heever S. P., 2016, *A&A*, **588**, A47

This paper has been typeset from a  $\text{\TeX}/\text{\LaTeX}$  file prepared by the author.